Micron 150 (2021) 103121

Contents lists available at ScienceDirect

Micron

journal homepage: www.elsevier.com/locate/micron

Quantitative analysis methods for studying fenestrations in liver sinusoidal endothelial cells. A comparative study

K. Szafranska [a,b,*], C.F. Holte [a], L.D. Kruse [a], H. Mao [a], C.I. Øie [a], M. Szymonski [b], B. Zapotoczny [a,c], P.A.G. McCourt [a]

[a] Department of Medical Biology, Vascular Biology Research Group, University of Tromsø (UiT), The Arctic University of Norway, Norway
[b] Centre for Nanometer-Scale Science and Advanced Materials, NANOSAM, Faculty of Physics, Astronomy, and Applied Computer Science, Jagiellonian University, Krakow, Poland
[c] Institute of Nuclear Physics, Polish Academy of Sciences, 31-342, Krakow, Poland

ARTICLE INFO

Keywords:
Quantitative analysis of LSEC porosity
Machine learning
Fenestrations
Liver sinusoidal endothelial cells
Atomic force microscopy
Super-resolution microscopy

ABSTRACT

Liver Sinusoidal Endothelial Cells (LSEC) line the hepatic vasculature providing blood filtration via transmembrane nanopores called fenestrations. These structures are 50−300 nm in diameter, which is below the resolution limit of a conventional light microscopy. To date, there is no standardized method of fenestration image analysis. With this study, we provide and compare three different approaches: manual measurements, a semi-automatic (threshold-based) method, and an automatic method based on user-friendly open source machine learning software. Images were obtained using three super resolution techniques – atomic force microscopy (AFM), scanning electron microscopy (SEM), and structured illumination microscopy (SIM). Parameters describing fenestrations such as diameter, area, roundness, frequency, and porosity were measured. Finally, we studied the user bias by comparison of the data obtained by five different users applying provided analysis methods.

1. Introduction

Liver Sinusoidal Endothelial Cells (LSEC) are the interface between the blood stream and the surrounding hepatocytes in the liver. Filtration is maintained by LSEC nanopores which are also known as fenestrations. Their diameter of 50−300 nm is crucial for size dependent passive transport of plasma soluble molecules (e.g., albumin, glucose, drugs) and small nanoparticles such as chylomicron remnants (Braet and Wisse, 2002). These nanopores are typically found in groups of 5–100 called sieve plates which are located mostly in the area outside the nuclear region. Fenestrations are dynamic structures that can react to various stimuli such as drugs or change in local environment (Braet and Wisse, 2002) and adapt their diameter and/or number within minutes or even seconds (Zapotoczny et al., 2019, 2017). Along with the passive transport of macromolecules via fenestrations, LSEC also participate in the clearing of circulating waste through active uptake via scavenging receptors. A diverse array of macromolecular waste material is constantly removed from the blood circulation by clathrin-mediated endocytosis (Sørensen et al., 2012). LSEC also play an active role in the clearance of circulating polyoma virus (Simon-Santamaria et al., 2014) and bacteriophages (Øie et al., 2020).

Both the number and diameter of fenestration are important for proper liver function. Defenestration – the loss of porous morphology is an early indication of liver fibrosis, which can cause atherosclerosis due to lack of filtration of lipoproteins from the blood stream (Rogers et al., 1992). It has been reported that porosity decreases in ageing and can be a main factor contributing for the need of increasing doses of drugs targeting hepatocytes (e.g. statins) that have to pass through the pores to reach their target (Le Couteur et al., 2002; Hunt et al., 2018a). Conversely, hepatocyte mediated detoxification of drugs from the plasma, requires porous LSEC – age related loss of porosity can result in drug doses, otherwise safe for young people, being toxic for the elderly. Moreover, hepatocytes regulate the glucose plasma concentration and LSEC are responsible for the passage of insulin (via fenestrations) to facilitate glucose disposal (Tsuchiya and Accili, 2013). All these aspects confirm that the lack of a healthy LSEC phenotype plays an important role in the development of many diseases. However, recent work has shown that the ageing related loss of LSEC fenestrations may be

* Corresponding author at: Vascular Biology Research Group (VBRG), University of Tromsø (UiT), Hansine Hansens veg 18, 9019 Tromsø, Norway.
E-mail addresses: szafranska.k.j@gmail.com, karolina.szafranska@uit.no (K. Szafranska).

https://doi.org/10.1016/j.micron.2021.103121
Received 28 March 2021; Received in revised form 1 July 2021; Accepted 14 July 2021
Available online 28 July 2021

reversible by repurposing a number of existing medicines (Hunt et al., 2018b, a). In addition, new nanomedicines show promise in this regard (Hunt et al., 2020b, 2021).

To date, in almost every article describing LSEC, the fenestration size is typically shown as a histogram of diameter distribution and/or mean value of fenestration diameter. Other parameters describing LSEC's porous morphology are fenestration frequency (number of fenestrations per area, less often per cell) and porosity (percentage of cell area covered by fenestrations). Altogether, these three features allow for complete evaluation and comparison between the LSEC phenotype in health and diseases, as well as after challenge with various drugs, with ageing, etc. However, the methods by which researchers obtain these data are often vaguely described. The lack of standardization results in cumbersome comparisons between the separate experiments conducted by different researchers.

Only a few studies proposed to standardize and automate the analysis of fenestrations using images obtained by different microscopy techniques. In 2015, Cogger et al. (2015) proposed a method for isolation, sample preparation and analysis using scanning electron microscopy (SEM). The authors suggested to manually mark the cell surface area and then measure the longest fenestration diameter using free access software such as Fiji/ImageJ (Schindelin et al., 2012). Although this method can be precise, it is time consuming and requires an assumption of fenestration circularity, which may bias the results. The magnification or pixel size issues resulted from poor image resolution are not discussed in the protocol. In 2018, Di Martino et al. (2018) proposed the analysis method for STED (Stimulated Emission Depletion) microscopy images of fenestrations using contour trace and macro programming to obtain semi-automatization of the process. The brief description suggests also that some manual steps are required. The authors made assumptions about fenestration circularity, but the exact roundness parameters for exclusion were not specified. Kong and Bobe (2021) proposed a well described semi-automated processing of human LSEC images obtained by Structured Illumination Microscopy (SIM). A Python based automated image processing macro utilizes an adaptive thresholding process and segmented images are further analysed to calculate both the number and diameter of fenestration. In 2017, we proposed the quantitative method for atomic force microscopy (AFM) image analysis of LSEC (Zapotoczny and Szafranska, 2017). Fenestration diameters were manually measured from high magnification images and, together with the manually counted fenestration number, then converted into porosity. The proposed method was precise, yet time consuming similarly to the other methods described above that involve manual measurements.

Recent developments in machine learning resulted in new possibilities for automatization or semi-automatization of the LSEC morphology analysis. Li et al. (2020) proposed an in house developed image recognition program based on a fully convolutional network for fenestration analysis. Unfortunately, many algorithms require programming skills in various programming languages, which is the main obstacle for the wide use of machine learning in biology. Recently, new software was developed with user friendly interfaces such as Weka Segmentation (Arganda-Carreras et al., 2017) or Ilastik (Berg et al., 2019). The combination of machine learning, basic image analysis and manual adjustments offers new ways to optimize the previously proposed methods and adjust them to sample size and precision needed for future experiments.

In this article we compare three different methods of image analysis: fully manual, semi-automatic (thresholding using ImageJ/Fiji) and automatic – machine learning (based on Ilastik software). We apply all three analysis methods for images obtained using each type of microscopy – AFM, SEM, and SIM. For clarity, both methods and results sections are divided according to the three imaging techniques. Finally, user bias is discussed based on the cross-correlation of image analysis performed independently by five researchers.

2. Materials and methods

2.1. Cell isolation

The cells were isolated as described in Zapotoczny and Szafranska (2017) for AFM and SIM (mouse LSECs) and in Mönkemöller et al. (2018) for SEM (cryopreserved rat LSEC). The experiments followed protocols approved by the local Animal Care and User Committees. Briefly, mice/rats were anesthetized using a mix of ketamine/xylazine and liver was perfused to remove blood and digested using Liberase™ (Roche, Germany). Thereafter, parenchymal cells were removed by a series of centrifugations. Mouse LSECs were isolated using immunomagnetic separation and CD146 conjugated magnetic beads (MACS, MiltenyiBiotec, Germany) while rat LSEC were separated by density gradient centrifugation (50/25 % Percoll gradient) followed by selective adherence to remove stellate cells and Kupffer cells, respectively. After separation, cells were seeded on glass coverslips and washed with media after 1 h incubation in 37 °C, 5 % CO_2, 5 % O_2 (cell culture media and surface coating specified for each technique below).

2.2. Sample preparation, imaging, and quantitative analysis

The differences in properties of the images obtained by each microscopy modality affect the analysis strategies. Therefore, each quantitative analysis is described separately for each imaging technique. For more detailed examples of the analysis see Supplementary Materials. The list of the parameters of interest can be found in Table 1.

2.2.1. Atomic Force Microscopy (AFM)

2.2.1.1. Sample preparation and imaging. In our analysis, we used images of samples prepared according to Zapotoczny and Szafranska (2017) and Mönkemöller et al. (2018). LSEC were cultured for 12−16 h on uncoated glass coverslips in EGM-2 full media (Lonza) and fixed for 2 min in 1 % glutaraldehyde in PBS and stored in PBS (with Mg^{2+}, Ca^{2+}) until imaging for up to two weeks. The measurements were performed using a JPK Nanowizard 3 AFM system (JPK Instruments AG, Germany) in PBS (with Mg^{2+}, Ca^{2+}) in a commercial liquid cell with the temperature control (25 °C). High magnification images were obtained using Quantitative Imaging mode with semi-soft (k = 0.03−0.06 N/m) triangular cantilevers with sharpened tips (radius <12 nm); low

Table 1
Parameters used for description of LSEC morphology.

Parameter	Definition	Unit
Cell area	(SEM/SIM) area of single cell surface (AFM) area of all cells in the image reduced by nuclei region of height above 700nm	nm^2 (μm^2)
Fenestration diameter	Max diameter – the longest diameter of single fenestration Min diameter – the shortest diameter of single fenestration For (semi-)automatic methods max and min diameter are calculated with the assumption of elliptical shape	nm
Roundness	$\frac{\text{min diameter}}{\text{max diameter}}$	0−1, unitless
Single fenestration area	(circularity assumption) $\pi \times \text{diameter}^2$ (elliptical assumption) $\pi \times \text{min diameter} \times \text{max diameter}$	nm^2
Total area of fenestrations	(Manual method, SI2) Number of fenestrations x fenestration diameter distribution ((Semi-)automatic methods) total detected area of fenestration	nm^2 (μm^2)
Porosity	$\frac{\text{total area of fenestrations}}{\text{cell area}} \times 100\%$	%
Fenestration frequency	$\frac{\text{number of fenestrations}}{\text{cell area}}$	$\frac{\text{No. of fen.}}{\mu m^2}$

magnification images of whole cells were imaged with contact mode and semi-soft triangular cantilevers with a regular tip (radius <60 nm). Precise imaging description and parameters such as loading force can be found in our previous work (Zapotoczny and Szafranska, 2017). Collected data were processed with JPK Data Processing Software and converted to tiff format for further analysis using ImageJ/Fiji.

2.2.1.2. Quantitative analysis.

1 Fenestration diameters

Single fenestration diameters were measured in three different ways from 26 high magnification images displaying a total of 625 fenestrations. A representative image is presented in Fig. 1A.

I Manual quantification was performed as follows: First, images were scaled to the scale bar individually for every image. Then, the shortest and the longest diameter of each fenestration were measured (minor and major axis respectively, assuming an elliptical shape of fenestration). Finally, the area of every pore was calculated with the assumption of an elliptical shape. The roundness parameter was defined as a ratio between the minor and major axes measured. Every fenestration was assigned with a number for further identification and comparison with another two methods. Holes on the edge of the image or clearly distorted i.e., not having a round shape or merged due to imaging or sample preparation artifacts were excluded.

II The semi-automatic method is based on the difference in contrast between the inside of fenestration and LSEC membrane. A simple threshold tool in Fiji was used to manually set cut off values for every independent image to ensure maximal precision (image from same imaging conditions are recommended when applying the same thresholding value to reduce bias). Next, the image was converted into a binary mask and then every fenestration was measured. Parameters such as fenestration area, fenestration diameter (min, max, mean), and roundness were calculated automatically (under "Analyze particles" tool in Fiji, size and circularity were set the same for all the images) and assigned to each fenestration according to the previously established order (for fenestration-by-fenestration analysis). Similarly to the manual quantification, the scale bar was used to adjust the scale for every image.

III The automatic method for the measurement of fenestrations is based on machine learning. Presented results were analyzed with Ilastik software. The algorithm was trained on a set of four representative images. A user teaches the software by marking parts of the image indicating the areas of fenestrations and the rest of the cell body area. Training is simple and takes about 30 min. Then, batch processing was applied to all 26 images to create simple segmentation binary masks (Fig. 1A, top). Finally, masks were analyzed using ImageJ/Fiji similarly to the semi-automatic method.

All 625 fenestrations were independently assigned with area, diameter (min, max, mean) and roundness obtained from three different quantitative methods and then compared.

2 Fenestration frequency and porosity

The fenestration frequency and porosity (see Table 1 for definitions) were measured from low magnification images of whole cells (Fig. 1B). 27 images of 40 μm × 40 μm size were analyzed. Initially, the image size was artificially converted (from 1024 × 1024 pixels to 2048 × 2048 pixels) with linear interpolation to digitally increase the resolution of an image ("Adjust Size" tool in Fiji). Artificially increased resolution does not bring any new information, however smaller pixel size is beneficial for better fenestration detection in all 3 analysis methods.

I Manual quantification was utilized in a two-step process. First, fenestrations were counted manually for the whole AFM images. Second, the cell area was calculated, excluding the background and nuclei areas. To achieve this, by using the 3D information about the topography of cells, regions of heights above 0.7–1.0 μm were excluded from analysis, by image contrast adjustment. We assumed that fenestrations can be formed only in flat areas of LSEC. Finally, the total area occupied by fenestrations, fenestration frequency, and porosity were calculated using the number of holes and mean diameter distribution measured from high magnification images (detailed description of calculation can be found in Supplementary information SI.1.).

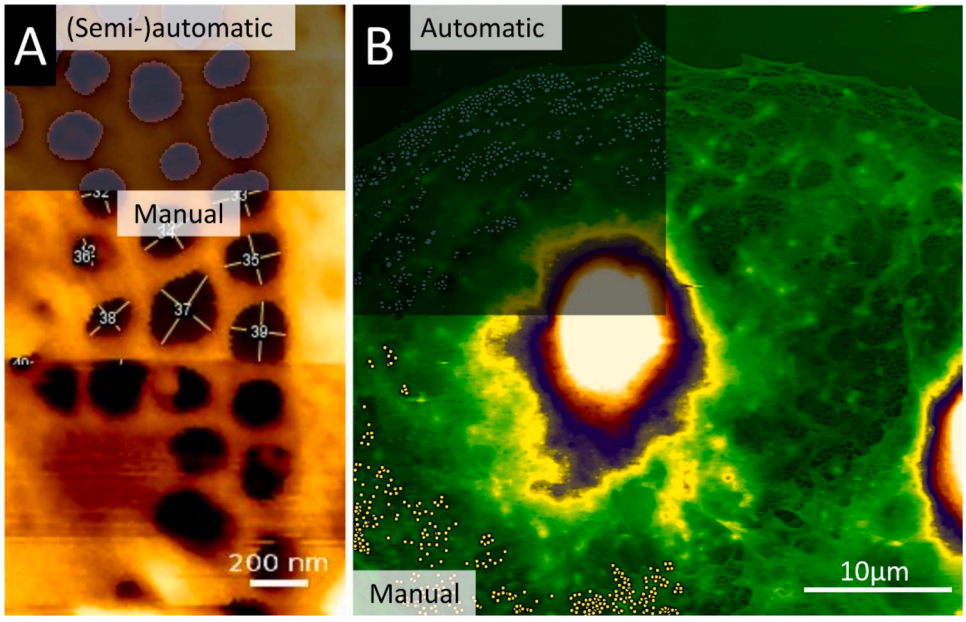

Fig. 1. Representation of the AFM image analysis. (A) High magnification AFM image of the sieve plate. Overlaid mask of fenestrations detected by (semi-)automatic methods and manually measured diameters are presented. Fixed cells were imaged using QI AFM mode and a sharp MSCT tip. (B) Low magnification AFM image of LSEC. Overlaid mask of detected fenestrations from the automatic method and marker points from manual fenestration counting are shown. Fixed cells were imaged using AFM contact mode and the MLCT tip.

II Simple thresholding could not be used for low magnification images due to the artefacts of AFM measurements that make the height (topography) images look curved/tilted. Built in image corrections are not sufficient and images require cumbersome analysis. Therefore, the semi-automatic method could not be applied to the low magnification AFM images.

III Automatic image analysis was successfully applied to measure fenestration number and area from low magnification AFM images. First, the program was trained on sets of four images (training time of around 1 h) and then all 27 images were analyzed using batch processing. Next, images were converted into simple segmentation binary masks and analyzed in ImageJ/Fiji. To avoid fenestrations merged together the watershed tool was used followed by particle analysis to exclude objects from outside of the fenestration range of 50−300 nm and circularity below 0.4. The remaining objects were automatically counted, and the total area measured to calculate porosity and fenestration frequency.

2.2.2. Nanoscopy – Structured Illumination Microscopy (SIM)

2.2.2.1. Sample preparation and imaging. Samples were prepared as previously described (Zapotoczny and Szafranska, 2017; Mönkemöller et al., 2018). Briefly, cells were seeded on fibronectin coated coverslips in RPMI-1640 medium (Sigma-Aldrich) and then fixed for 10 min with 4 % formaldehyde (FA) in PBS and stored in PBS containing 0.1 % FA. Before imaging, cells were stained using CellMask Green (ThermoFisher) 1:1000 dilution in PBS for 30 min and then mounted onto glass slides using Vectashield antifading mounting media (Vector Labs). Images were obtained using a commercial SIM microscope (OMX Blaze system, GE Healthcare) with a 60x 1.42NA oil-immersion objective (Olympus). 3D-SIM image stacks of 2−3 μm were acquired with a z-distance of 125 nm and with 15 raw images per plane (five phases, three angles). Raw datasets were computationally reconstructed using SoftWoRx software (GE Healthcare) and z-projections in tiff format were prepared for further analysis.

2.2.2.2. Quantitative analysis (Fenestration diameter, fenestration frequency and porosity). Initially, the image size was converted from 1024 × 1024 pixels to 2048 × 2048 pixels, with linear interpolation, using the adjust size tool in Fiji to digitally increase the resolution of the image.

I The scale was adjusted to the size of the image of 40.96 μm × 40.96 μm and 300 fenestrations were manually measured from the top right quarter of each of 20 images. For every fenestration, both the smallest and the largest diameters were measured to calculate mean values. For calculation of fenestration frequency, the cell area was measured using the threshold tool in ImageJ/Fiji (fenestrations area including) and fenestrations were manually counted (Fig. 2 Manual). Porosity was calculated using fenestration diameter distribution and the number of fenestrations individually for every image (for detailed calculations see Supplementary information SI.1.).

II For the semi-automatic method, images were converted into binary masks using the threshold tool with manually adjusted values for each image. A watershed function was then applied to avoid exclusion of merged fenestrations, and only objects within the fenestration size range were saved ("Analyse particles" Fiji tool, 50−300 nm diameter and circularity above 0.4). Finally, fenestration diameter, the total area and number of fenestrations were measured and used to calculate porosity and fenestration frequency (Fig. 2 Semi-automatic).

III The machine learning based automatic method was used for fast image processing. After training on four images (training time of about 1 h) all 20 images were processed and converted into simple segmentation binary masks in tiff format (Fig. 2 Automatic). Further analysis was the same as for the semi-automated method described above (analyse particles, size dependent object exclusion).

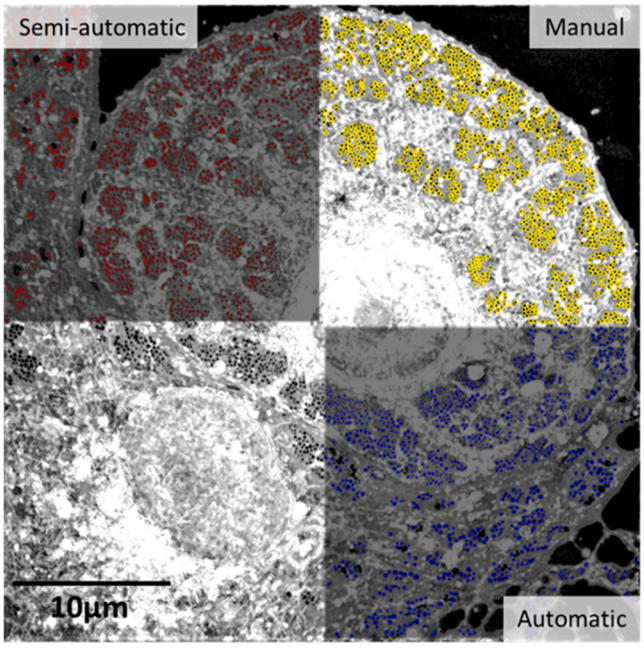

Fig. 2. Representative analysis of SIM image of LSEC stained with CellMask Green. Red - fenestrations detected by semi-automatic method, blue – fenestrations detected by automatic machine learning method, yellow marks – fenestrations counted manually.

2.2.3. Scanning Electron Microscopy (SEM)

2.2.3.1. Sample preparation and imaging. Samples were prepared as previously described (Mönkemöller et al., 2018). LSEC were seeded for 3 h on fibronection covered glass coverslips in RPMI-1640 medium (Sigma-Aldrich) and then fixed and stored in a mix of 4 % formaldehyde and 2.5 % glutaraldehyde in cacodylic buffer. Samples were then processed with 1 h treatment with freshly made 1 % tannic acid in PHEM buffer, 1 h of 1 % OsO_4 in H_2O, dehydrated in ethanol gradient (30 %, 60 %, 90 % for 5 min each, 5 times for 4 min in 100 % ethanol, and incubated twice for 10 min in hexamethyldisilane (HMDS), then left overnight to evaporate. Before imaging, samples were mounted on metal stubs using carbon tape and silver glue to reduce charging and then sputter coated with 10 nm gold/palladium. A commercial SEM system (Sigma, Zeiss) was used for imaging with a 2 kV electron beam. Low magnification images (Fig. 3B) were obtained from 5 different areas of the sample with 20 images of single cells in total. High magnification images (Fig. 3A, ~6.5 nm/pixel) were taken for each of the 20 cells.

2.2.3.2. Quantitative analysis.

1. Fenestration diameters

Contrast and brightness were adjusted for every image and the scale was set according to the scale bar.

I Fenestrations were manually measured from 20 high magnification images; assuming elliptical shape, both the smallest and the largest diameter (along minor and major axis respectively) were measured and then used for the calculation of the area and roundness.

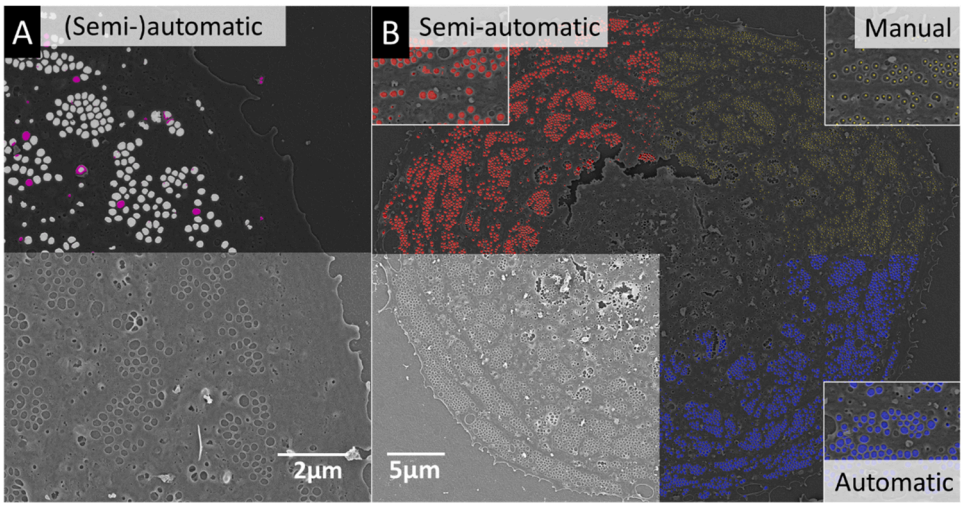

Fig. 3. Representation of the SEM image analysis. (A) High magnification of LSEC imaged using SEM. The upper panel of the image represents the overlaid mask of detected fenestration by semi- and automatic methods (white) or automatic only (magenta). (B) Low magnification of LSEC imaged using SEM. Red - fenestrations detected by semi-automatic method, blue – fenestrations detected by the automatic machine learning method, yellow – fenestrations counted manually.

II The second semi-automatic method based on the Fiji threshold function consists of few steps (detailed example in Supplementary information SI.2.). First, the contrast was adjusted to better visualize the edges of fenestrations and the image was inverted. Next, the threshold was manually set using the Huang algorithm to the point where single fenestrations but not their surrounding edges were covered. Images were then converted into binary masks and objects larger than 300 nm or smaller than 50 nm and with roundness below 0.4 were excluded. Every fenestration was then automatically measured and parameters such as area, diameters (min, max, mean) and roundness were calculated.

III For fast image processing, machine learning was applied. First, the algorithm was trained using four images (training time of about 2 h) and then all 20 images were processed and converted into simple segmentation binary images. Fenestrations were then measured the same way as described for the semi-automated method.

2. Porosity and fenestration frequency

I Fenestrations were manually counted (Fig. 3B, yellow) and the cell area was calculated from the manually marked cell shape. The total area of fenestrations was calculated using fenestration number and previously measured diameter distribution from high magnification images (details in SI.1.).

II The semi-automatic method was applied with parameters adjusted for every image individually as for the high magnification images described above (contrast adjustment, inversion, threshold and particle analysis exclusion by size) (Fig. 3B red). The total area and number of fenestrations were automatically measured after scale adjustment and used for the calculation of porosity and fenestration frequency.

III For automatic analysis, the algorithm was trained using five low magnification SEM images and then all 20 images were processed. Simple segmentation binary images were then analyzed using ImageJ/Fiji similarly to the semi-automated method.

2.3. User comparison

Five individual users with different experience with image analysis were asked to analyze one high magnification SEM and nine SIM images. For the SEM image, each user was asked to manually measure the same 700 marked fenestrations, set the scale by measuring the scale bar and perform analysis using semi-automatic and automatic methods according to the descriptions above. Then each of the 700 marked fenestrations were assigned with parameters (area of single fenestration, fenestration diameters (min, max, mean), and fenestration roundness). For SIM images, all participants were asked to manually count fenestrations from nine whole images and then analyze all images using semi-automatic and automatic methods as described above. The parameters were measured by five different users using three different analysis methods. Results were cross-correlated between each other (every single user with every other user).

2.4. Statistics

All statistical analyses were performed using OriginPro software (OriginPro 2021, OriginLab Corp., Northampton, MA). The total numbers of analysed cells and fenestrations are summarized in the Table 2. For porosity and frequency parameters, the comparison between the methods was based on the relation between the (semi-) automatic methods and manual (standard) approach. The linear correlation is necessary for the method to be useful in the experiments with expected changes in selected parameters. Therefore, linear regression was fitted to the data with the R^2 coefficient describing linearity (the closer to 1 the more linear) and slope (tangent of the angle) describing the correlation between the values. A slope of 1 is preferred as the change in porosity/frequency measured by the (semi-) automatic and manual methods would remain the same even if the absolute values vary. Slopes lower or higher than 1 mean under- or over-estimation, respectively.

Table 2
Total number of analysed images per imaging technique.

Imaging technique	Image Magnification	Number of images/cells	Number of measured fenestrations	Pixel size [nm]
AFM	High	26	(M,S-A, A) 625	4–6
	Low	27		20
SIM	Low	20	(M) 6 000 (S-A) 60 000 (A) 63 000	20
SEM	High	20	(M) 8 100 (S-A, A) 16 000	6–7
	Low	20		18–20

M – manual, S-A- semi-automatic, A - automatic.

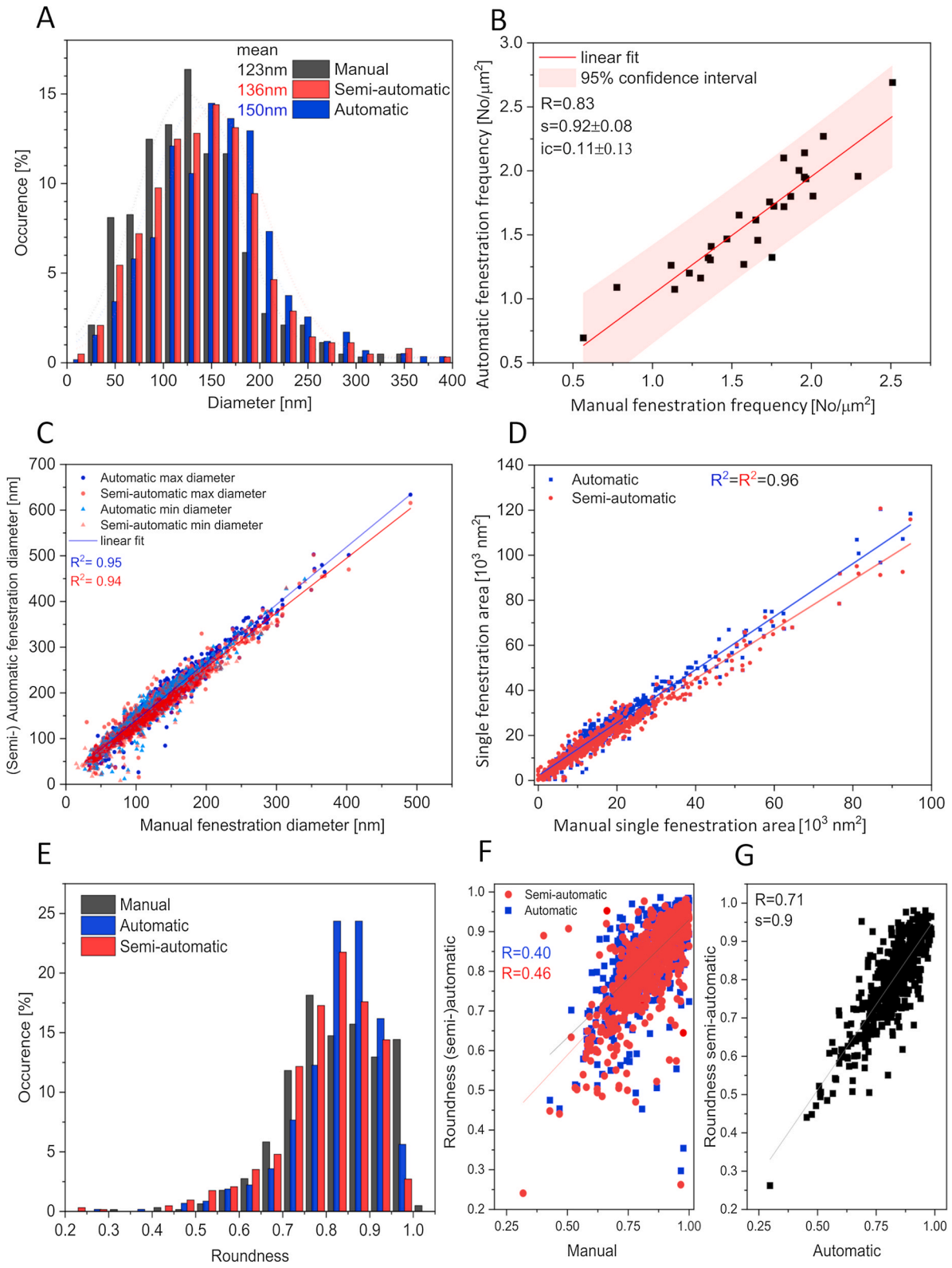

Fig. 4. Analysis of AFM images. (A) Histogram of fenestration diameter distribution. The dotted lines represent fitted Gaussian curves from which the mean values were calculated. Data comes from 625 fenestrations from 26 high magnification images of sieve plates (see Fig. 1A). (B) Correlation of fenestration frequency calculated using Automatic and Manual counting. Each dot represents a single image (see Fig. 1B), 27 images in total. S - slope of the fitted linear function, ic - intercept. (C) comparison of single fenestration diameter measured manually and automatically with the assumption of elliptical fenestration shape. Max, min diameter – major and minor axis of the ellipse. (D) comparison of single fenestration area measured manually and automatically. (C, D) each dot represents a single fenestration measured by 3 different techniques. (E) Distribution of fenestration roundness measured by different techniques (roundness = ratio of min to max diameter). (F, G) correlation of roundness parameter between manually and automatically measured fenestrations.

3. Results and discussion

In this section, the terms Manual, Semi-automatic and Automatic are used for the 3 quantitative analysis methods described in detail in the Materials and Methods section

3.1. AFM image analysis

Fenestration diameter distribution obtained from 26 high magnification AFM images show differences between the three analysis methods (Fig. 4A). Gaussian curves were fitted to calculate the mean diameter and the width of the distribution. The smallest mean diameter of 123 nm was obtained from manually measured data, semi- and automatic methods gave values of 136 nm and 150 nm, respectively. The larger diameter for non-manual methods may be related to the fenestration edge detection. Manual measurement is based on contrast and user judgement and may vary between the images. For semi- and automatic methods, the diameter is calculated back from the measured areas of single fenestrations with the assumption of circularity. Moreover, the detection of fenestrations by machine learning may require detection of the edge of the hole and it could therefore increase the total area and diameter of fenestration. This issue is related to the pyramidal shape of the AFM tip which may influence the intensity gradient corresponding with the height on the fenestration edge (more information about the AFM tip shape problems for fenestration measurement can we found in Zapotoczny and Szafranska (2017)). A pixel size of 4−6 nm would explain that difference of 13/27 nm, which correlates with 2–4 pixels between the manual and (semi-)automatic methods (Fig. 4A).

Individual analysis of each of the 625 fenestrations provides a comparison of each of the three analysis techniques for each pore. Fig. 4C shows the linear relation between the manually measured min and max diameters and the (semi-)automatic method calculated data. The fitted linear regression presents a good correlation of $R^2 = 0.94$ and 0.95 for the automatic and semi-automatic methods, respectively. The slope of the regression for both methods was 1.2 and the intercepts of 16 nm and 10 nm for the automatic and semi-automatic methods, respectively. Both the slope above 1 and the intercept values confirm that the non-manual methods detect fenestrations as larger than the manual data, however, the good linear correlation makes the measurement comparable between the samples with differences in fenestration size. The same results have been observed for fenestration-by-fenestration analysis of the areas of single pores (Fig. 4D). The linear regression slope of 1.1 and $R^2 = 0.96$ show a good linear correlation.

Most of the previously published articles dealing with the measurement of LSEC morphology assumed circularity of fenestrations. Here we show that the roundness parameter – the ratio between minimum and maximum diameter, concentrates about the value of ~0.85 for all methods (Fig. 4E). Interestingly the distribution of the manual measurements is wider and the number of nearly circular fenestrations (0.95-1) is much higher than for (semi-)automatic methods. Moreover, the comparison of roundness of single fenestrations between the three methods shows a correlation between automatic and semi-automatic (Fig. 4G) but not between manual and automatic methods (Fig. 4F). This result may suggest the user bias towards a more circular shape as the choice of min/max diameter is subjective. The roundness distribution from the automatic and semi-automatic methods is very similar and a slight increase towards more round fenestrations correlates well with the assumption that the machine learning algorithm detects the edges of the holes equally enlarging both min and max diameters and therefore increasing the roundness parameter.

The fenestration frequency calculated using automatic methods shows good correlation with the manual measurement (Fig. 4B). Almost all measured data lay within 95 % confidence interval and slope of 0.92 with $R^2 = 0.83$ indicate linear correlation.

3.2. SIM image analysis

Twenty LSEC SIM images were analyzed in three different ways. The comparison between the manual method and the (semi)automatic methods (Fig. 5A) showed a linear correlation with R^2 values of 0.85 and 0.82, respectively. The correlation for SIM is similar to the AFM images which it is enough to be useful for comparison of data from different treatment groups. There are no significant differences in the measured numbers of fenestration per image between various analysis methods (Fig. 5B). Fenestration frequency was not calculated due to difficulties in the detection of cell boundaries. The Cell Mask dyes are a group of cell membrane dyes that provide great contrast needed for detection of fenestrations but further analysis and calculations can be optimized for single cells only on non-confluent samples where only a single cell is visible in the field of view of the microscope. Alternatively, cells can be separated manually. For samples with tight cell monolayers, the cell area can be normalized according to the visible number of cells for porosity/fenestration frequency calculations by subtraction of the mean area of nuclei (10 μm is a good approximation of diameter of LSEC nuclei).

Fig. 5C shows the differences in the distribution of diameters. The semi-automatic method shifted distribution towards a larger apparent fenestration size with a mean value of 178 nm. Automatic and manual methods gave similar results with mean diameters of 138 nm and 130 nm, respectively. Machine learning showed a high number of small pores below 75 nm which may be an artifact of the detection algorithm and can be optimized by the increased training time. For all methods objects smaller than 50 nm were excluded. A pixel size of 20 nm is not sufficient for the detection of holes below 50 nm due to Nyquist's sampling criterion. The mean diameter values were calculated as centers of the fitted Gaussian distribution curves to compensate for this. The difference between semi-automatic and the other methods can be biased by the manual adjustments of the cut-off intensity value. The threshold must be set individually for every image so changes towards both smaller and larger diameters can be introduced by the users. It is not possible to use a fixed value as the intensity in the perinuclear area varies between the cells and would induce artifacts that influence the segmentation more than the manual adjustment.

Similarly to the data from the AFM images, the roundness parameter was calculated with the assumption of fenestration elliptical shape. The shift towards a more circular shape can be observed for manual measurements which is consistent with the previous observation, most probably resulting from the user bias. Also, the roundness values concentrate around a value of 0.9 for SIM images compared to 0.82 for AFM images. This difference is connected with the imaging technique – raw SIM images require reconstruction which will make small objects at the edge of achievable resolution appear more round in shape due to Wiener filtering (part of the SIM reconstruction algorithm). Adjustment of the image size using bilinear interpolation makes the shape even more circular. Nevertheless, the benefits of the decreased pixel size, which allows better precision of the quantitative analysis, outweigh the downsides.

3.3. SEM image analysis

Twenty high magnification SEM images were quantitatively analyzed using three different methods. Comparisons between manual and (semi)automatic techniques showed differences in the shape of mean diameter distribution (Fig. 6A). Mean fenestration size was calculated from the manually measured min and max diameters or for (semi-)automatic methods calculated from the detected areas, assuming circularity of holes. Only manually measured values had a simple Gaussian distribution with the center at 175 nm. The other two methods show the results with at least double Gaussian shape peaks; the first one being within the regular fenestration size range with centers at 178 nm and 191 nm for semi-automatic and automatic methods respectively,

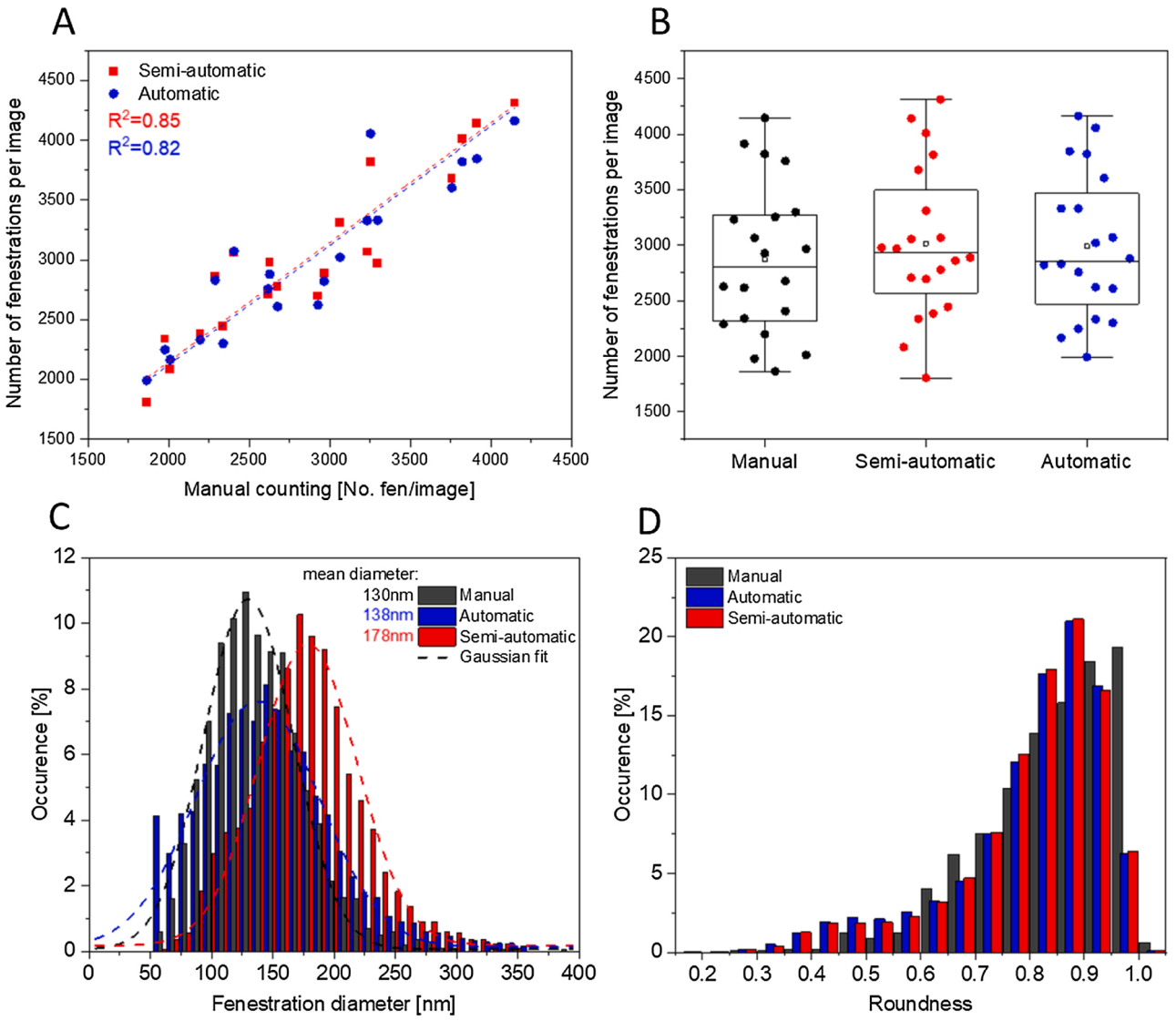

Fig. 5. Analysis of SIM images. (A) Correlation between manually and automatically counted fenestrations. Each dot represents a single image (see Fig. 2), 20 images in total. (B) Comparison of fenestration frequency between the studied groups. (C) Distribution of fenestration diameter. The dashed line represents fitted Gaussian curve from which the average value was calculated (tip of the curve). Fenestrations smaller than 50 nm were excluded due to a pixel size of 20 nm. The total number of fenestrations measured – 6 000, 60 000, 63 000 from manual, semi-automatic and automatic methods respectively. (D) Distribution of the roundness parameter calculated from measured fenestrations.

and the second maximum with centers at 100 nm and 120 nm. The additional detected objects are identified on the images as non-transmembrane protrusions in the cell membrane, most probably endocytic vesicles arising from the prominent endocytic properties of LSECs. Their size and contrast, being similar to fenestrations, make them impossible to be separated from fenestrations using threshold or Ilastik analysis, however, they can be removed from further calculations and analysis using the multi-peak Gaussian curve fitting or by cutting off all the objects below a certain size. The first approach requires more time as it should be adjusted for every cell/image but interferes less with the data. The second approach can be automated to a cut-off value set in the middle of the two maxima, but it can significantly affect the results if changes in fenestration diameters towards smaller values are expected (two peaks overlapping).

Fenestration-by-fenestration analysis with three different methods shows a good linear correlation between manual and (semi)automatic measurements with $R^2 = 0.95–0.96$ and a slope of 1. The automatic compared to the semi-automatic approach causes a 16 nm shift towards larger apparent fenestration size and area of 2300 nm^2. Similarly to the analysis of the AFM images, the machine learning algorithm is detecting the edge of the holes resulting in the systematic error with the value connected to the pixel size. This error would not affect the comparison between the treatment groups with expected changes in diameter but should be taken into consideration for comparison between data calculated with different methods of analysis.

Porosity and fenestration frequency were calculated from low magnification images. Both semi-automatic and automatic methods show a linear correlation of the values of porosity when compared with manual measurements, $R^2 = 0.89$ and 0.91 (Fig. 6D). However, the slopes of the linear regression are 0.63 and 0.9 respectively. The difference in slope suggests that the semi-automatic method is underestimating the value of calculated porosity. The difference in slope values between the methods can be more pronounced with the increase of cell porosity due to drug treatment. As a result, smaller changes in cell porosity can be wrongly assigned as not significant. The smaller intercept of linear regression of the semi-automatic compared to the automatic method makes it more similar to manual measurement, however, the difference in slope is more important for the usefulness as a tool for

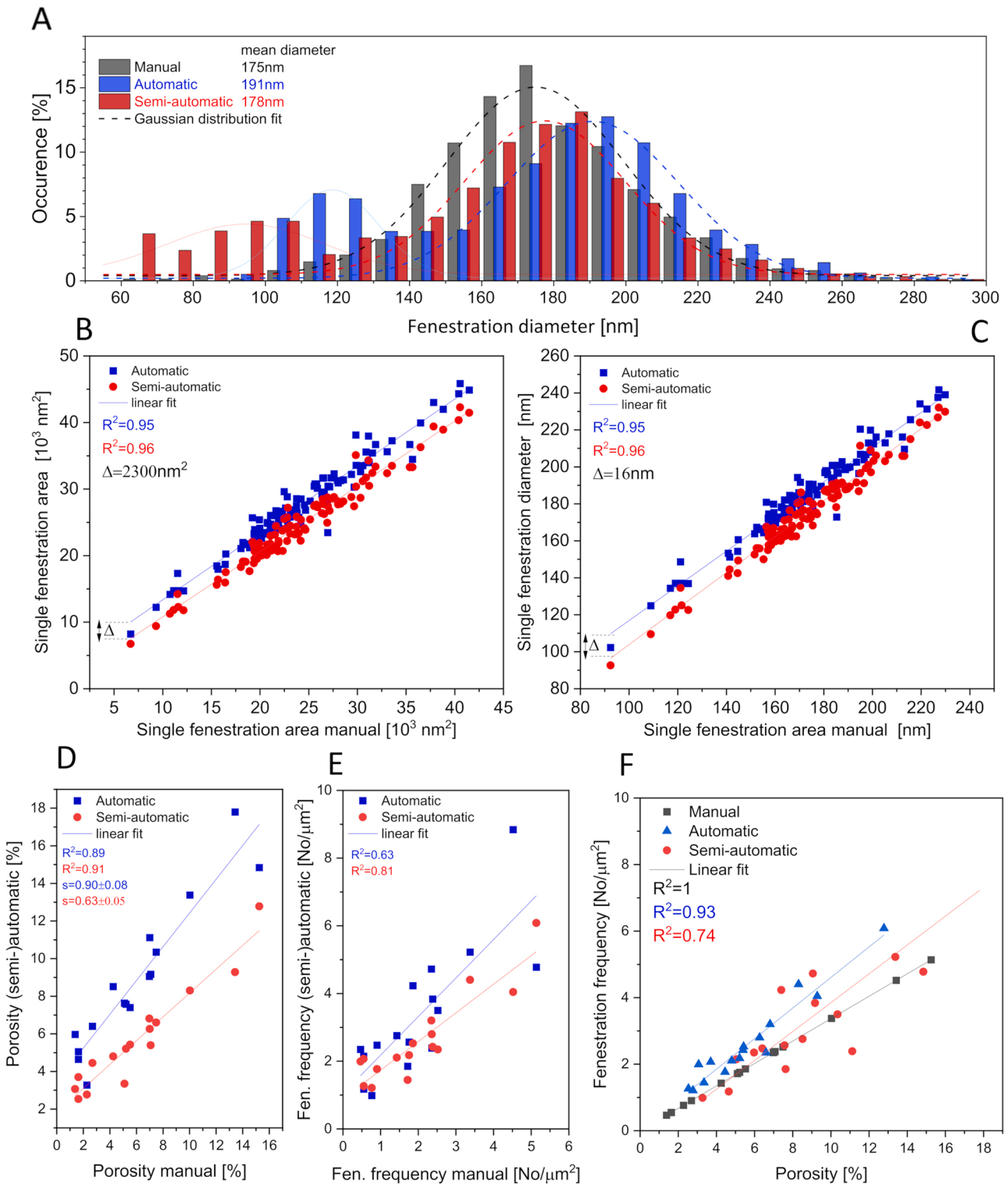

Fig. 6. Analysis of SEM images. (A) Fenestration diameter distribution measured from high magnification SEM images (see Fig. 3A). The dashed line represents fitted Gaussian curves, for semi-automatic and automatic methods a multi-peak fit was used to exclude the non-fenestration objects (thin line Gaussian curve). The total number of fenestrations measured – 8 100 from 20 images/cells for manual measurement and 16 000 from 20 images/cells for (semi-)automatic methods. Correlation of single fenestration area (B) and diameter (C) between manual and automatic methods. Δ – intercept between fitted linear functions. Comparison of porosity (D) and fenestration frequency (E) between manual and automatic methods. Each point represents a single image (see Fig. 3B), total number of images – 18. (F) the relation between frequency and porosity measured using different methods.

comparison between treatment groups.

Fenestration frequency showed a weaker linear correlation than porosity with $R^2 = 0.63$ and 0.81 for Ilastik and threshold respectively (Fig. 6E). These results correlate with the detection of the small fenestration-like objects shown as a second maximum on diameter distribution (Fig. 6A). Because of the small size of these structures, they do not significantly affect porosity, but their number is significant compared to detected fenestrations and this influences fenestration

Table 3
Parameters of fenestrations measured by 3 different methods from SEM images.

Parameter		Manual	Semi-automatic	Automatic
Area	Average [nm^2]	26,926 ± 2140	26,818 ± 443	26,488 ± 3767
	User comp. [%]	1.25 ± 12	0.10 ± 1.8	3.45 ± 22.6
Max diameter	Average [nm]	199 ± 7	201 ± 1.8	200 ± 13
	User comp. [%]	0.34 ± 5.25	0.03 ± 0.86	0.79 ± 10.29
Min diameter	Average [nm]	168 ± 7	166 ± 1.4	165 ± 12
	User comp. [%]	0.46 ± 6	0.03 ± 1	1.10 ± 12
Mean	Average [nm]	184 ± 7	184 ± 1.4	182 ± 13
	User comp. [%]	0.30 ± 5.7	0.02 ± 0.87	0.8 ± 10.9
Roundness	Average	0.849 ± 0.011	0.828 ± 0.001	0.830 ± 0.009
	User comp. [%]	0.000 ± 0.015	0.000 ± 0.001	0.000 ± 0.019

±SD; user comp. = comparison between users.

frequency. The above proposed approaches of removing these structures may help to reduce the effect on fenestration frequency and enable comparison between the groups if changes in frequency are expected to be independent of porosity changes (for example changes in fenestration diameter may compensate for the difference in fenestration number and show no changes in porosity). The comparison between porosity and fenestration frequency among the studied methods (Fig. 6F) shows a good correlation for manual measurement due to the direct connection between these parameters – the fenestrated area used to calculate porosity is calculated from the number of fenestrations. The automatic method shows a good linear correlation with R^2 of 0.93 while the semi-automatic method presents R^2 of 0.74 which points to the influence of detected fenestration-like objects in the calculation of fenestration number.

3.4. User comparison

To compare the differences between users and study user bias, sets of SIM and SEM images were analyzed by five researchers with different levels of imaging experience, from beginner to advanced user.

3.4.1. SEM

Firstly, 700 fenestrations from Fig. 3A were individually measured (fenestration-by-fenestration) by five users using the three studied methods and then the parameters were cross-correlated between all the users. Next, mean values were calculated for every user and the average was calculated for each method. Interestingly, the average values of parameters were similar for all techniques (Table 3). However, differences between the users (Fig. 7) and SD values of the cross-correlation show significant differences among the users. The biggest deviation is observed with the automatic method; the cross-correlation parameter for a single fenestration area was only 3.5 %, but the standard deviation of over 20 % suggested significant differences between the users. One of the main reasons for that may be the specificity of the machine learning algorithm. Each user trained the software independently and small differences can lead to different ways of detecting fenestrations. Every fenestration on a SEM image has a visible, high contrast edge which can be included or excluded from the detected area. Differences between the calculated mean values of the diameter (Fig. 7B) for manual and automatic methods are of about 6−7 nm which is similar to the pixel size of this image - 6.5 nm. The semi-automatic method is intensity and contrast based and therefore, less sensitive to user preferences about the fenestration edge. Fenestrations are detected due to high contrast edges characteristic for SEM images - steep edges give a higher signal compared to a flat cell surface or substrate in the fenestration lumen. This hypothesis was confirmed by merging binary images of detected fenestration from automatic and semi-automatic methods showing rings around the holes (see Supplementary information SI.3). Small differences in fenestration roundness among the users using the semi-automatic method (Fig. 7C) also suggest that the shape of the detected holes is the least biased by this method. A shift towards a more circular shape (roundness value closer to 1) is observed for manual measurements which (consistent with previous observations) confirms the influence of the assumption of circularity by the users.

3.4.2. SIM

Nine SIM images were analyzed independently by five users with the three methods. Each image was then cross-correlated between all users and (semi-)automatic methods were compared with manual counting.

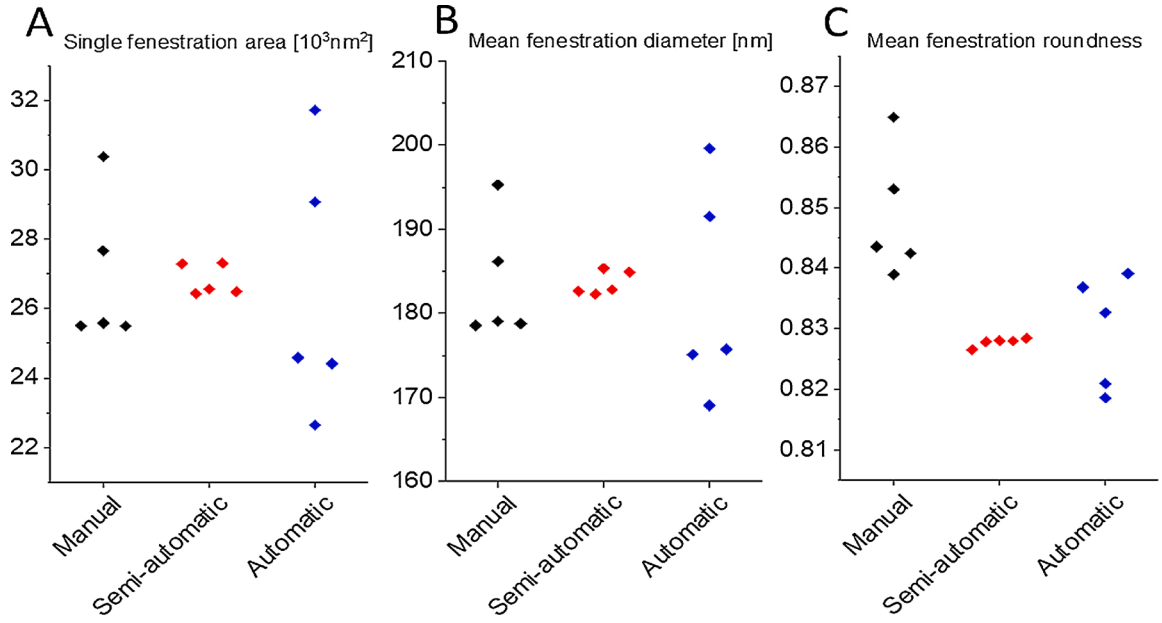

Fig. 7. Comparison of analysis methods between the users. Each point represents one user and the mean value of the presented parameter calculated from 700 measured fenestrations from SEM image.

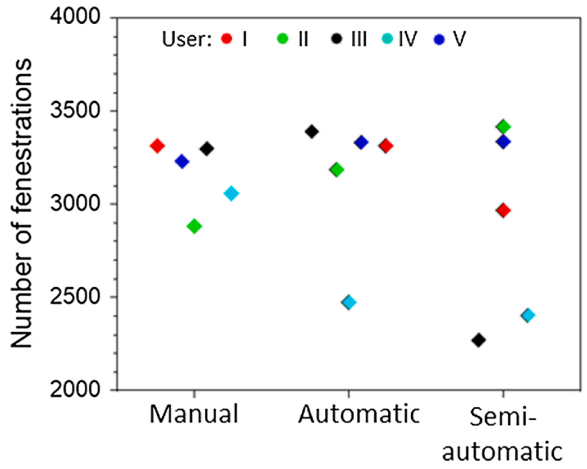

Fig. 8. Comparison between users' measurements of fenestrations number using three different techniques for one of the analysed SIM images.

Table 4
Comparison of fenestration number between the users and analysis methods for SIM images.

Change in fenestration number compared to manual counting [%]			
User	Semi-automatic	Automatic	Manual
I	10.1 ± 13	10.2 ± 12	
II	18.5 ± 9	8 ± 11	
III	−7.4 ± 15	−5.9 ± 11	
IV	−4.8 ± 13	−11.5 ± 12	
V	−4.5 ± 14	3.5 ± 13	
Cross correlation between users [%]	1.9 ± 9.5	3.3 ± 12	0.17 ± 11

The mean value of fenestration number per image was similar among the users (0.2–3.3 %), however, the difference between users within one method was about 10−12 %. An example of one of the analyzed images (Fig. 8) shows the differences between the users and methods. Manual counting has the smallest variation while (semi-)automatic methods present a wider range of calculated numbers. The main source of differences between the users using (semi)automatic methods is the large pixel size which causes the merging of fenestrations within one sieve plate during segmentation. Lowering the threshold or retraining the machine learning software leads to the presence of undetected fenestrations while the watershed function, used to split the merged holes, leads to splitting single fenestrations which causes an elevated number of detected objects (Table 4). The decision is made by each user and if it is standardized, the error can be minimized.

3.5. Discussion

In this study we investigated the use of three methods for quantitative analysis of LSEC images: manual measurement or counting of fenestrations, a semi-automatic threshold-based method and an automatic machine learning-based method. All three techniques have their advantages and disadvantages, mainly time efficiency at the cost of accuracy. The manual method was, until recently, the standard way of fenestration analysis due to the lack of proper software to semi-automate or automate the process. It was considered to be the gold standard, but the lack of scoring description prevents a proper comparison between results from different studies. Recently, attempts to apply home-made algorithms and machine learning have been reported (Di Martino et al., 2018; Kong and Bobe, 2021; Li et al., 2020), but their application requires a certain level of programming skills not available to every researcher. Here we report two methods which can be easily applied to experimental data where differences in fenestration diameter and/or number are expected.

The efficiency of each method depends mainly on the number of samples which is directly correlated with the time needed for analysis. This can be optimized in each study by designing experiments that would give minimum but sufficient sets of data for statistical analyses. The most time consuming is the manual method but the poor image quality or high number of artifacts may prevent the use of other, faster techniques. User comparison showed also that there is significant user bias for manual measurements so all analyses should be performed by one single user, ideally blind to the sample id. If there is a need for data analysis to involve more than a single person, the threshold method would introduce the smallest bias for fenestration size measurements. Fenestration frequency and porosity show similar differences among the users for all three methods so the choice can be based on to the quality of the images.

The data from all three imaging techniques suggests that the precision of both (semi-)automatic methods is similar and linear correlation allows us to use them for comparison of the parameters between experimental groups. All experiments where changes in fenestration size and/or number are expected can be analyzed using the semi-automatic or automatic method. However, the porosity calculated from SEM images using the semi-automatic method may seem underestimated. The comparison between the manual and semi-automatic methods shows a linear correlation with a slope below 1, which indicates that some fenestrated areas are not detected in the cells with higher porosity/higher number of fenestrations

The machine learning software includes a batch processing feature where, after training, tens or even hundreds of images can be automatically analyzed. The only limitation is the computer processing power which affects the speed. The main disadvantage of this approach is the requirement of images with similar contrast and brightness. In practice, each sample or group of samples may require adjustments for these parameters, and depending on the number of samples, this may reduce the time advantage over the semi-automatic method. Although, the threshold-based approach requires manual adjustment of the cut-off value for each image segmentation but still, the large number of fenestrations is analyzed for each manual step. It is a significant advantage over the fully manual approach, where single manual step gives information about only one fenestration.

For fenestration size measurements, both (semi-)automatic methods showed a systematic error that needs to be taken into consideration. The source of this error was identified and connected with the edge of the fenestration detection, related to the pixel size of the image. For the automatic method, the batch processing of all images using the same trained algorithm would solve this problem. For manual and semi-automatic methods inclusion/exclusion must be decided before the analysis.

4. Conclusions

All three proposed methods can be applied for fenestration analyses, but the best method should be selected based on the following criteria: the available imaging technique, the achievable quality of the images, the time for the analysis and the predicted outcome in measured

Table 5
Comparison of properties of the three methods of quantitative analysis.

Property	Manual	Semi-automatic	Automatic
Speed	− − − −	+	++
User bias	−/+	+	−/+
Accuracy - fenestration number	++	−	+
Accuracy - porosity	+/−	+	+
Accuracy - diameter	+/−	++	+
Artifacts sensitive	++	− −	−/+
Image quality sensitive	++	− −	−/+
User friendly	++	++	+

parameters. The pros and cons of the three selected methods are listed in Table 5.

We emphasize the need for small-scale pilot experiments to assess both the best imaging technique as well as the predicted range of changes in the LSEC morphology parameters. The time invested in the analysis of preliminary results will lead to the best possible protocol for further analysis. The combination of more than one analysis method can also be beneficial, for example, the best accuracy of diameter measurement was shown with the semi-automatic method while the number of fenestrations is most precisely detected manually.

The main limiting factor – time – can be overcome by automation, which is getting easier with the developments of new and more precise software and ongoing advancements in the field of microscopy. The results of this study show that the semi-automatic and automatic methods can be a timesaving alternative for the standard manual approach, but considerations of suitable methods are needed prior to application.

The choice of the best analysis method has to be based on the quality of every experimental data set. We suggest to first focus on obtaining the best possible image quality, within reasonable imaging time. For the fenestration size measurements, we recommend use of semi-automatic or automatic method. Automatization allows measurement of thousands of fenestrations at the same time compared to manual measurement of tens of fenestrations; it provides a better statistical overview and removes user bias manifesting as an increase in the roundness parameter. For the porosity and fenestration frequency measurements we recommend the use of the automatic method as it is the most time efficient simultaneously processing of many images. If the image quality is poor, and artifacts do not allow the use of automatic methods, the manual approach may be necessary. When using (semi-)automatic methods we recommend using the manual method for small data sets as a reference, especially if the changes in porosity or fenestration frequency between the experimental groups are small.

The above strategies for scoring LSEC porosity using SEM, SIM and AFM imaging can also be applied to other super resolution imaging modalities applied to LSEC, e.g. dSTORM (Mönkemöller et al., 2014; Mao et al., 2019) or STED (Di Martino et al., 2018). These latter two methods have the highest reported optical resolution, at 10−20 nm. (Semi-)Automation of the LSEC porosity scoring process, in combination with current and new developments in super-resolution imaging, will accelerate the evaluation of LSECs in health, disease and aging, thus aiding to development of therapies that reverse the effects on LSEC defenestration, a key phenotypic feature in various diseases and ageing.

Declaration of Competing Interest

The authors declare no competing interest.

Acknowledgements

This work received funding from the European Union's Horizon 2020 research and innovation programme under the Marie Sklodowska-Curie grant agreement no. 766181, project "DeLIVER" and Research Council of Norway, Grant no. 288565 "NANO2021". This work was supported by the Polish National Science Centre under the "SYMFONIA 3" project, grant agreement no. UMO-2015/16/W/NZ4/00070.

The authors would like to thank Randi Olsen and Tom-Ivar Eilertsen from Advanced Microscopy Core Facility at UiT for the electron microscopy expertise and Deanna Wolfson for the help with SIM imaging.

Appendix A. Supplementary data

Supplementary material related to this article can be found, in the online version, at doi:https://doi.org/10.1016/j.micron.2021.103121.

References

Arganda-Carreras, I., et al., 2017. Trainable Weka Segmentation: a machine learning tool for microscopy pixel classification. Bioinformatics 33 (15). https://doi.org/10.1093/bioinformatics/btx180.

Berg, S., et al., 2019. Ilastik: interactive machine learning for (Bio)Image analysis. Nat. Methods 16 (12). https://doi.org/10.1038/s41592-019-0582-9.

Braet, F., Wisse, E., 2002. Structural and functional aspects of liver sinusoidal endothelial cell fenestrae: a review. Comp. Hepatol. 1 (1) https://doi.org/10.1186/1476-5926-1-1.

Cogger, V.C., et al., 2015. A standardized method for the analysis of liver sinusoidal endothelial cells and their fenestrations by scanning electron microscopy. JoVE 98. https://doi.org/10.3791/52698.

Di Martino, J., et al., 2018. STED microscopy: a simplified method for liver sinusoidal endothelial fenestrae analysis. Biol. Cell 110 (7). https://doi.org/10.1111/boc.201800016.

Hunt, N.J., et al., 2018a. Novel targets for delaying aging: the importance of the liver and advances in drug delivery. Adv. Drug Deliv. Rev. 135 https://doi.org/10.1016/j.addr.2018.09.006.

Hunt, N.J., et al., 2018b. Manipulating fenestrations in young and old liver sinusoidal endothelial cells. Am. J. Physiol. – Gastrointest. Liver Physiol. 316 (1) https://doi.org/10.1152/ajpgi.00179.2018.

Hunt, N.J., et al., 2020a. The effects of metformin on age-related changes in the liver sinusoidal endothelial cell. J. Gerontol. - Ser. A Biol. Sci. Med. Sci. 75 (2) https://doi.org/10.1093/gerona/glz153.

Hunt, N.J., et al., 2020b. Rapid intestinal uptake and targeted delivery to the liver endothelium using orally administered silver sulfide quantum dots. ACS Nano 14 (2). https://doi.org/10.1021/acsnano.9b06071.

Hunt, N.J., et al., 2021. Quantum dot nanomedicine formulations dramatically improve pharmacological properties and alter uptake pathways of metformin and nicotinamide mononucleotide in aging mice. ACS Nano 15 (3). https://doi.org/10.1021/acsnano.0c09278.

Kong, C., Bobe, S., et al., 2021. Multiscale and multimodal optical imaging of the ultrastructure of human liver biopsies. Front. Physiol. 12 https://doi.org/10.3389/fphys.2021.637136.

Le Couteur, D.G., et al., 2002. Hepatic pseudocapillarisation and atherosclerosis in ageing. Lancet 359 (9317). https://doi.org/10.1016/S0140-6736(02)08524-0.

Li, P., et al., 2020. Characterizing liver sinusoidal endothelial cell fenestrae on soft substrates upon AFM imaging and deep learning. Biochim. Biophys. Acta 1864 (12). https://doi.org/10.1016/j.bbagen.2020.129702.

Mao, H., et al., 2019. Cost-efficient nanoscopy reveals nanoscale architecture of liver cells and platelets. Nanophotonics 8 (7). https://doi.org/10.1515/nanoph-2019-0066.

Mönkemöller, V., et al., 2014. Imaging fenestrations in liver sinusoidal endothelial cells by optical localization microscopy. Phys. Chem. Chem. Phys. 16 (24) https://doi.org/10.1039/C4CP01574F.

Mönkemöller, V., et al., 2018. Primary rat LSECs preserve their characteristic phenotype after cryopreservation. Sci. Rep. 8 (1) https://doi.org/10.1038/s41598-018-32103-z.

Øie, C.I., et al., 2020. Liver sinusoidal endothelial cells contribute to the uptake and degradation of entero bacterial viruses. Sci. Rep. 10 (898) https://doi.org/10.1038/s41598-020-57652-0.

Rogers, G.W.T., et al., 1992. Decreased hepatic uptake of cholesterol and retinol in the dimethylnitrosamine rat model of cirrhosis. Liver 12 (5). https://doi.org/10.1111/j.1600-0676.1992.tb00581.x.

Schindelin, J., et al., 2012. Fiji: an open-source platform for biological-image analysis. Nat. Methods 9. https://doi.org/10.1038/nmeth.2019.

Simon-Santamaria, J., et al., 2014. Efficient uptake of blood-borne BK and JC polyomavirus-like particles in endothelial cells of liver sinusoids and renal Vasa recta. PLoS One 9 (11). https://doi.org/10.1371/journal.pone.0111762.

Sørensen, K.K., et al., 2012. The scavenger endothelial cell: a new player in homeostasis and immunity. Am. J. Physiol. 303 (12) https://doi.org/10.1152/ajpregu.00686.2011.

Tsuchiya, K., Accili, D., 2013. Liver sinusoidal endothelial cells link hyperinsulinemia to hepatic insulin resistance. Diabetes 62 (5). https://doi.org/10.2337/db12-1296.

Zapotoczny, B., Szafranska, K., et al., 2017. Quantification of fenestrations in liver sinusoidal endothelial cells by atomic force microscopy. Micron 101. https://doi.org/10.1016/j.micron.2017.06.005.

Zapotoczny, B., et al., 2017. AFM reveals dynamic morphology of fenestrations in living liver sinusoidal endothelial cells. Sci. Rep. 7 (7994) https://doi.org/10.1038/s41598-017-08555-0.

Zapotoczny, B., et al., 2019. Tracking fenestrae dynamics in live murine liver sinusoidal endothelial cells. Hepatology 69 (2). https://doi.org/10.1002/hep.30232.